Published in final edited form as:
J Bone Miner Res. 2020 August ; 35(8): 1572–1581. doi:10.1002/jbmr.4009.

Intervertebral Disc Degeneration Is Associated With Aberrant Endplate Remodeling and Reduced Small Molecule Transport

Beth G Ashinsky[1,2,3], **Edward D Bonnevie**[1,2,†], **Sai A Mandalapu**[1,2,†], **Stephen Pickup**[4], **Chao Wang**[3], **Lin Han**[3], **Robert L Mauck**[1,2], **Harvey E Smith**[1,2], **Sarah E Gullbrand**[1,2]

[1]Translational Musculoskeletal Research Center, Corporal Michael Crescenz VA Medical Center, Philadelphia, PA, USA

[2]McKay Orthopaedic Research Laboratory, Department of Orthopaedic Surgery, University of Pennsylvania, Philadelphia, PA, USA

[3]School of Biomedical Engineering Science and Health Systems, Drexel University, Philadelphia, PA, USA

[4]Department of Radiology, University of Pennsylvania, Philadelphia, PA, USA

Abstract

The intervertebral disc is the largest avascular structure in the body, and cells within the disc rely on diffusive transport via vasculature located within the vertebral endplate to receive nutrients, eliminate waste products, and maintain disc health. However, the mechanisms by which small molecule transport into the disc occurs in vivo and how these parameters change with disc degeneration remain understudied. Here, we utilize an in vivo rabbit puncture disc degeneration model to study these interactions and provide evidence that remodeling of the endplate adjacent to the disc occurs concomitant with degeneration. Our results identify significant increases in endplate bone volume fraction, increases in microscale stiffness of the soft tissue interfaces between the disc and vertebral bone, and reductions in endplate vascularity and small molecule transport into the disc as a function of degenerative state. A neural network model identified changes in diffusion into the disc as the most significant predictor of disc degeneration. These findings support the critical role of trans-endplate transport in disease progression and will improve patient selection to direct appropriate surgical intervention and inform new therapeutic approaches to improve disc health.

Address correspondence to: Sarah E Gullbrand, Translational Musculoskeletal Research Center, Corporal Michael Crescenz VA Medical Center, Philadelphia, PA 19104, USA. sgullb@pennmedicine.upenn.edu.

[†]EDB and SAM contributed equally to this work.

Authors' roles: BGA, RLM, HES, and SEG designed the research. BGA, EDB, SAM, SP, CW, HES, and SEG conducted the research. BGA, EDB, SAM, CW, and SEG analyzed the data. BGA, LH, HES, RLM, and SEG interpreted the data. BGA and SEG compiled the manuscript with assistance and approval from all authors. BGA and SEG accept responsibility for the integrity of the data analysis.

Additional Supporting Information may be found in the online version of this article.

The peer review history for this article is available at https://publons.com/publon/10.1002/jbmr.4009.

Disclosures
RLM is the editor of *JOR Spine*. All other authors state that they have no conflicts of interests.

Keywords

ANIMAL MODELS; BONE REMODELING; INTERVERTEBRAL DISC DEGENERATION; SMALL MOLECULE DIFFUSION; VASCULARITY

Introduction

The intervertebral discs of the spine are composed of a viscous, proteoglycan- and water-rich central region, the nucleus pulposus (NP), encased circumferentially by the annulus fibrosus (AF), which consists of collagen fibrils oriented in alternating lamellae.(1) This composite structure allows the healthy disc to bear loads up to five times body weight during normal activities, while still permitting spinal motion.(2) Surrounding the discs superiorly and inferiorly are vertebral endplates, which anchor the disc to the adjacent vertebral bodies. The vertebral endplates are layered structures, composed of semiporous thickened cancellous bone (0.6 to 1 mm thick) and hyaline cartilage (0.2 to 0.8 mm thick), aligned parallel to the vertebral surface.(3) The boney region has a higher hydraulic permeability than the cartilaginous endplate, yet the porosity of both components is highest at the central region, representing the endplate-NP interface(3) (Fig. 1A). {FIG1}

The disc is the largest avascular structure in the human body and receives all of its nutrients and metabolite exchange from the vascular network in the adjacent vertebral bodies. (4–6) Whereas the outer AF is also sparsely vascularized, the boney endplate provides the predominant route for nutrient transport into the disc.(7) The vascular supply to the vertebral bodies originates from the segmental arteries, which branch from the abdominal aorta, forming an arterial gridlike network deep within the bone.(8) The vertebral capillaries form branches and terminate as vascular buds adjacent to the cartilaginous endplate. Thus, nutrients and waste products must diffuse from these vessels and sinusoids across the endplates to maintain disc cell activities.(9) This diffusional limitation creates a challenging biochemical microenvironment within the center of the NP, characterized by a high concentration of lactate and low concentration of glucose and oxygen.(10,11)

With aging or after injury, degeneration of the intervertebral disc and adjacent spinal tissues is common.(12) Disc degeneration has been implicated as a causative factor in back pain, which is the leading cause of disability and health care expenditures worldwide.(13) Disc degeneration is classically characterized by the degradation of NP and AF matrix components, which compromises the load-bearing properties of the disc.(12) This mechanical insufficiency is frequently associated with pathology, including a reduction in disc height, NP herniation, and/or spondylosis.(12) The etiology of disc degeneration remains poorly understood but is likely multifactorial, involving synergistic interactions between mechanical and biological mechanisms, including genetics and NP cell catabolic activities. (14–16)

An additional factor that likely contributes to disc degeneration is a reduction in nutrient supply and waste product exchange within the avascular disc. The mechanisms contributing to reduced transport to and from the disc remain unclear, yet alterations to the boney endplate, cartilaginous endplate, and spinal vasculature likely play a role. Previous work has focused mainly on the contribution of the cartilaginous endplate, demonstrating that calcification and dehydration of the cartilage endplate reduce tissue diffusivity.(17) Such alterations would likely reduce oxygen and glucose concentrations and decrease pH within the disc, which has been shown in cell culture systems to compromise NP cell viability and matrix production.(18,19) The boney endplate and vasculature are the source of small molecule transport into the disc, yet alterations to these spinal structures during degeneration remain understudied. Confounding data exist regarding changes to the boney endplate, with some studies demonstrating that sclerosis occurs and others suggesting a loss of bone density with increasing severity of degeneration.(6,20–22) Occlusion of the vertebral arteries has been correlated with degeneration;(23) however, alterations to the small vessels immediately adjacent to the disc have not been previously investigated. Despite this previous work, the precise relationships between endplate and vascular remodeling, in vivo disc perfusion, and degeneration have yet to be established. Therefore, the purpose of the current study was to perform a comprehensive and quantitative in vivo analysis of the dynamic structure–function changes in the vertebral endplate at multiple length scales to determine how remodeling of this structure may be associated with altered diffusion into the disc in vivo during degeneration. We hypothesized that changes in the endplate would be evident early in degeneration and that a reduction in small molecule diffusion into the disc would be a primary predictor of degenerative state.

Materials and Methods

Study design and animal surgery

The study design is shown in Fig. 1A. Fifteen male skeletally mature New Zealand White rabbits (~3 kg, ~3 months of age, Charles River Laboratories, Wilmington, MA, USA) underwent standard perioperative protocols for surgery at the University of Pennsylvania. The anesthesia protocol was defined by the Institutional Animal Care Use Committee (IACUC) guidelines at the University of Pennsylvania for rabbit surgery. Using aseptic techniques, four consecutive lumbar discs between L_2 to L^3 and L_6 to L_7 were punctured with a 16G needle, as previously described.(24,25) Four levels of the lumbar spine per animal were punctured to reduce the number of animals required for this study, consistent with IACUC guidelines and previous studies in the field.(25,26) After surgery, animals were single housed and allowed to resume normal cage activity. At postoperative weeks 4, 8, and 12, rabbits were euthanized, and lumbar motion segments (vertebral body–IVD–vertebral body) were isolated for analysis. Because of the destructive nature of some assays, motion segments at each time point were randomly divided into two groups for experimental procedures. One group of animals was administered bone fluorochrome labels for microscopy and then underwent contrast-enhanced T_1 magnetic resonance imaging (MRI), microcomputed tomography (μCT), and then atomic force microscopy (AFM). The second group of animals underwent vascular perfusion, T_1 MRI, and paraffin histology. Uninjured lumbar motion segments from each animal served as experimental controls for each assay. A chart detailing the number of levels and independent animals utilized for each outcome measure is shown in Supplemental Fig. S1.

Fluorochrome labeling

Calcein (20 mg/mL) was dissolved in isotonic sodium bicarbonate solution and administered subcutaneously to a subset ($n = 3$ of the rabbits), 6 weeks before euthanasia, in order to fluorescently label new mineral deposition green.(27,28) Alizarincomplexone (15 mg/mL) was dissolved in isotonic sodium bicarbonate and administered subcutaneously to the same rabbits (25 mg/kg), 2 weeks before euthanasia, in order to fluorescently label tissue that is mineralizing red.

Fluorochrome imaging

Sagittal cryosections were taken at 10 μm thick using Kawamoto's film method.(29) Fluorescent imaging was performed at ×10 (Nikon [Tokyo, Japan] Eclipse) to visualize and quantify calcein (green) and alizarin (red) labels within the vertebral endplate between the growth plate and disc ($n = 3$–9 motion segments per group). Images of the calcein and alizarin labels were thresholded in ImageJ and the fluorescent signal area of each label in the vertebral endplate was quantified.

Magnetic resonance imaging

At each experimental time point, rabbits were administered 0.3 mmol/kg of the small molecule, non-ionic MRI contrast agent gadodiamide (Omniscan [GE Healthcare, Piscataway, NJ, USA], MW = 573).(30–32) Thirty minutes after contrast agent delivery, animals were euthanized, and the lumbar motion segments ($n = 4$–11 per time point) were subjected to T_1 mapping at 4.7 T using an inversion recovery sequence and a custom solenoid coil. A series of coronal T_1 images were obtained and the T_1 relaxation time within the NP and AF were calculated,(33) which is inversely proportional to the concentration of gadodiamide in the tissue.

Microcomputed tomography

Motion segments ($n = 4$–6/group) were subjected to μCT scanning (Scanco [Bruttisellen, Switzerland] μCT50) at 10 μm isotropic resolution. A volume of interest between the growth plate and disc was manually contoured to quantify bone volume fraction and trabecular morphometry parameters, including trabecular number, thickness, and spacing.

Atomic force microscopy

After μCT, motion segments ($n = 4$–6/group) were embedded in optimal cutting temperature media and cryosectioned in the sagittal plane at 50 μm using the Kawamoto film method.(29) AFM of the soft tissue adjacent to the vertebral body at the EP-AF and EP-NP interfaces was carried out using microspherical tips ($r = 12.5$ μm, k~1 N/m, 10 μm/s indentation rate) in phosphate-buffered saline with protease inhibitors. Indentation was performed at ≥12 locations in each region in each sample to account for the inhomogeneity of each region. The effective indentation modulus (E_{ind}) was calculated by fitting the loading force-displacement curve to a finite thickness-corrected Hertzian model.(34) The E_{ind} (MPa) was normalized to average control E_{ind} values in each region, and the data presented in Results are represented as a ratio of E_{ind} Degenerative/E_{ind} Control.

Microvascular analysis

Immediately after euthanasia in 3 animals at 12 weeks post-puncture, the descending aorta was isolated, ligated proximally, and catheterized distally, with the inferior vena cava opened to permit outflow. Then 1000 mL of saline supplemented with heparin (100 U/kg) was injected into the aortic catheter to clear the vasculature. The aorta was subsequently injected with 80 mL of microFil silicone rubber solution (Flow Tek, Boulder, CO, USA) to fill the vessels.(35) The lumbar spine was harvested after allowing the microFil to cure for 1 hour at room temperature. Spinal motion segments ($n = 8$ punctured, $n = 4$ control) were then fixed and decalcified before μCT analysis. A rectangular region of the endplate (~4 mm in width) adjacent to the NP was manually sectioned and subjected to μCT scanning (Scanco μCT50) at 2 μm isotropic resolution to quantify the volume fraction of the sample perfused with microFil. The microFil volume fraction of the endplate adjacent to punctured discs was normalized to the microFil volume fraction of the endplate from the adjacent, healthy control disc of each animal, so as to account for any variations in perfusion technique between animals.

Histology

Additional motion segments were fixed in 10% neutral-buffered formalin (Sigma-Aldrich, St. Louis, MO, USA), decalcified (Formical 2000; StatLab, McKinney, TX, USA), processed into paraffin, and sectioned at 10 mm thick in the sagittal plane. Midsagittal sections were stained with the rapid Mallory-Heidenhain trichrome stain,(36) which stains bone matrix pink, erythrocytes in the vasculature orange, and unmineralized collagen blue, and imaged using bright-field microscopy. Erythrocyte staining was thresholded in ImageJ, and vessel area and number were quantified for each sample(31) ($n = 3–5$ motion segments per time point). Additional slides were stained with either Alcian blue/ picrosirius red for proteoglycan and collagen, or hematoxylin and eosin (H&E) for cellular morphology. Stained slides were used for histology grading(37) (total 0–500) of AF organization (0–100), AF-NP border acuity (0–100), NP matrix (0–100) and cellularity (0–100), and EP structure (0–100) (Supplemental Table S1) by two blinded, independent observers on three to five motion segments per experimental group.

Second harmonic generation (SHG) imaging

Collagen localization and organization was assessed through SHG imaging using a Nikon A1 multiphoton microscope with 880 nm excitation, as previously described.(38) For each sample ($n = 2$ motion segments per time point), z-stacks of slides stained with Alcian blue/ picrosirius red were obtained over the 10 μm thickness. Z-stacks were imported into ImageJ and projected into an average intensity projection.

Statistical analysis

Statistical analyses were performed in GraphPad [La Jolla, CA, USA] Prism 7. Statistical significance was defined as $p < 0.05$. Data were tested for normality using the Shapiro–Wilk normality test. If the sample size was insufficient to test for normality, data were assumed to be non-normally distributed. For normally distributed data, significant differences in quantitative outcomes (ratio of indentation modulus, bone morphometry, vessel area, vessel number, and % T_1 reduction) across experimental groups (controls, 4 weeks, 8 weeks, 12 weeks) were assessed via a one-way ANOVA with Tukey's multiple comparison test. For non-normally distributed data, significant differences were assessed using the Kruskal-Wallis test with Dunn's multiple comparisons test. For calcein and alizarin fluorescence quantification, significant differences compared with controls were assessed via a Mann–Whitney test. For microFil data, significant differences in microFil volume fraction adjacent to degenerative discs (compared with controls within the same animal) were assessed using a two-tailed paired *t* test.

Neural network modeling

Quantitative outcomes from this study were combined with outcomes from our previously published work characterizing disc degeneration in the rabbit puncture model(24) to yield a total of 23 quantitative input parameters, from 29 different rabbits (42 total input samples), for neural network modeling. Input parameters included measures of MRI for disc health (NP T2, AF T2) and trans-endplate diffusion (% T_1 reduction NP), macroscale (neutral zone (NZ) modulus, NZ range of motion (ROM), compressive modulus, compressive ROM, total ROM, creep strain), and microscale (inner AF E_{ind}, outer AF E_{ind}, EP-AF E_{ind}, EP-NP E_{ind}) biomechanical function, bone morphometry parameters (bone volume fraction [BV/TV], trabecular [Tb.] number, Tb. thickness, Tb. spacing), biochemical composition (NP GAG content, AF GAG content, NP collagen content, AF collagen content), and endplate vascularity (% microFil and vessel area). In the case where certain assays were not performed across the same motion segment, an average value of the assay outcome at the particular time point was assigned.(39) These parameters were used as inputs (predictors) into a feedforward neural network model, using the multilayer perceptron (MLP) algorithm, with one hidden layer containing six neurons (each containing an activation function),(40) for classification of total histology score (SPSS Modeler, IBM Corp., Armonk, NY, USA). Training of the MLP was performed on iterations of 75% of the data set using backpropagation, and testing was performed on the remaining 25% of the samples. The weights and bias terms were optimized by minimizing the cross-entropy loss (cost) function through the gradient descent algorithm, and the resulting values were propagated through each layer of the network such that each neuron was assigned an error value (bias term) and each input was assigned a weight that reflects its contribution to the output. Pearson correlation coefficients were also calculated using the same data set for all combinations of variables (Supplemental Tables S2 and S3).

Results

Annular puncture induces progressive disc degeneration

To study the interactions between vertebral endplate remodeling, trans-endplate transport, and disc degeneration, an in vivo rabbit disc puncture model was utilized (Fig. 1A). Animals were euthanized at 4, 8, and 12 weeks after surgery, and vertebral body-disc-vertebral body spinal motion segments were harvested for analysis. After needle injury, degeneration of the disc was evident and progressed with time post-injury. These changes included a loss of disc height, disorganization of the AF, and anterior osteophyte formation, consistent with our previous work(24) and other reports using this model.(25,41–43)

Marked remodeling occurs in the boney and cartilaginous endplates during degeneration

Concomitant with this macroscopic degeneration of the disc itself, marked remodeling occurred within the boney and cartilaginous endplates adjacent to the degenerating disc. To investigate alterations to the structure of these soft tissue interfaces, SHG imaging was used to visualize collagen density and organization at these locations. SHG showed progressive thickening of the cartilaginous endplate adjacent to the NP, accompanied by increased collagen deposition at this interface, particularly at 12 weeks (Fig. 1B). Assessment of the microscale function of this remodeling tissue with AFM demonstrated a mean 851% increase in indentation modulus at 12 weeks compared with control. The ratio of indentation modulus (E_{ind} Degenerative/E_{ind} Control) at the EP-NP interface was significantly increased at 12 weeks (Fig. 1C) compared with 4 weeks ($p = 0.008$) and 8 weeks post-puncture ($p = 0.001$). At the interface between the AF and boney endplate, SHG illustrated significant disorganization of the lamellar architecture, most notably at 4 and 8 weeks (Fig. 1D). These structural changes were associated with a mean 700% increase in the ratio of indentation modulus of this region at 12 weeks post-puncture (Fig. 1E) compared with controls, although no significant differences were observed across time points post-puncture.

Along with interfacial soft tissue remodeling, changes in bone morphometry of the vertebral endplate was evident soon after degeneration was initiated, as quantified by µCT (Fig. 2A). {FIG 2} Generally, bone volume fraction increased in the vertebral endplate adjacent to punctured discs over time, with significant differences observed between the intact controls and the 12 weeks post-puncture group ($p = 0.0004$) and between the 4 and 12 week post-puncture groups ($p = 0.01$) (Fig. 2B). Trabecular thickness in the vertebral endplate increased as early as 4 weeks post-puncture and remained elevated at 8 and 12 weeks ($p = 0.0001$) compared with controls (Fig. 2C, D). Likewise, trabecular spacing decreased ($p = 0.008$) by 12 weeks compared with controls (Supplemental Fig. S2).

To further elucidate the dynamics of endplate bone remodeling, a subset of animals was administered calcein and alizarin complexone at 6 and 10 weeks post-puncture, respectively, to fluorescently label newly deposited mineralized bone.(27,28) Incorporation of these labels was visualized at 12 weeks and showed an increase in fluorochrome incorporation in the boney endplate adjacent to punctured discs compared with healthy controls (Fig. 2E and Supplemental Fig. S3). Quantification indicated significant increases in both calcein (Fig. 2F) and alizarin (Fig. 2G) incorporation adjacent to punctured discs compared with controls ($p = 0.001$ and $p = 0.009$, respectively).

Endplate vasculature is altered with disc degeneration

Next, we evaluated how the observed boney remodeling impacted vascularity in the endplate, the primary route for molecular transport into the disc. Qualitative and quantitative analysis of Mallory-Heidenhain trichrome-stained(36) histology sections indicated that vessel area and number (adjacent to the NP) were increased at 4 and 8 weeks post-puncture ($p = 0.01$ and $p = 0.009$, respectively), followed by reductions in both parameters at 12 weeks post-puncture (Fig. 3B, C). {FIG3}

To further assess alterations to the endplate vasculature in three dimensions across the depth of the vertebral body, the spinal vasculature of a subset of animals was perfused with a radiopaque compound, microFil(35) (Fig. 3D), for visualization by μCT after decalcification (Fig. 3E). Qualitatively, there appeared to be less perfusion of microFil to the endplate adjacent to the NP of degenerative discs at 12 weeks compared with the adjacent, healthy control disc of the same animal (Fig. 3E). Quantitatively, there was a significant (47%, $p =$ 0.0008) reduction in microFil volume fraction adjacent to degenerative discs at 12 weeks post-puncture compared with adjacent healthy controls (Fig. 3F).

Small molecule transport into the disc is reduced in degenerative discs

To determine how the remodeling of the endplate bone and vascularity with degeneration affected small molecule diffusion into the disc, animals at each time point were administered the small molecule, non-ionic contrast agent, gadodiamide, before euthanasia, followed by immediate quantitative T_1-mapping via MRI.(30,31) Gadodiamide is a T_1 shortening agent, and thus the percent reduction in the T_1 relaxation time (discs without gadodiamide versus those with gadodiamide, at each time point) provides a quantitative measure of small molecule diffusion into the disc (Fig. 4A, B). {FIG4} Within the NP, gadodiamide diffusion into the disc progressively decreased and was significantly lower at 12 weeks compared with healthy controls (p = 0.0001, Fig. 4C). Diffusion into the AF, however, was significantly reduced at 4 weeks post-puncture (p = 0.01), followed by a return to control levels (Fig. 4D).

Disc degeneration is predicted by reduced transport into the disc

To further elucidate the contribution of endplate remodeling to disc degeneration, we utilized a machine-learning approach to define which structural and/or functional change was most important for predicting degeneration. To do so, blinded histologic scoring (Supplemental Fig. S2 and Supplemental Table S1) of disc degeneration at each time point was performed,(38) yielding a single score for each sample (Fig. 5A {FIG5} and Supplemental Fig. S4) at each time point. Quantitative outcome metrics from the current study (assessing endplate bone and vascular remodeling and diffusion) were combined with outcomes from a previous study(24) detailing the structural and functional alterations to the disc itself across length scales. A feedforward neural network model was constructed using the 23 quantitative structure–function measurements as input values (features) to predict the histology score (target outcome) for each motion segment (Fig. 5B). By training on this data set, each feature was assigned a weight, indicating its importance in the model for predicting the histology score (95.1% classification accuracy) (Fig. 5C). This model identified $\% T_1$ NP reduction (the measure of small molecule diffusion into the disc) as the feature with the highest weight. The next most important features were the micromechanical properties (E_{ind}) of the outer AF and EP-AF interfaces, followed by NP collagen content (indicating NP fibrosis), and neutral zone range of motion (a macroscale mechanical measure indicating altered NP function). Of the top eight predictors of histology score in the neural network model, seven of these also had strong correlations (Pearson correlation coefficient > 0.5) with histology score (Supplemental Table S3).

Discussion

The intervertebral discs of the spine are the largest avascular structures in the body, and cells at the center of the human disc can be up to 6 mm away from the nearest nutrient supply of the vasculature in the vertebral endplate.(9) A decrease in the already limited disc transport has therefore been suggested as a potential contributor to the initiation and progression of disc degeneration. However, the timing and mechanism by which this occurs remains unclear. The results from this study provide in vivo evidence that substantial remodeling of the vertebral bone, diminished vascularity, and stiffening of the disc interfaces occur during early degeneration, followed by reduced small molecule diffusion into the disc at later time points.

With time following surgically induced degeneration in this rabbit model, significant increases in mineralization and bone volume fraction of the vertebral endplate were observed. Adjacent to the vertebral bone, the soft tissue interface between the NP and boney endplate stiffened, becoming thicker and containing denser collagen. The accurate quantification of indentation modulus across biologic tissue interfaces is challenging, as spatial resolution is limited by the contact area generated by AFM tip radius. Additionally, the values obtained for the modulus are affected by distance from the interface and the stiffness of adjacent tissues.(44) As we have used a tip radius of 12.5 μm, and the rabbit cartilage endplate is approximately 50 μm, the AFM measurements here likely represent the moduli of a combination of the tissues at the respective interfaces between the NP, AF, and the vertebral body. Additionally, as these tissues remodel post-puncture, the magnitude of the contribution of the stiffnesses of the adjacent tissues on the measured indentation modulus may change. That said, when probing the same regions over time post-puncture, substantial increases (5× to 15×) in the apparent indentation modulus were observed, suggestive of marked remodeling of the tissue at this location. This may influence transport into the disc, as previous work has established correlations between cartilage endplate diffusivity and tissue composition, and tissue composition and mechanical properties.(18,45) Further work is needed to establish a direct correlation between local tissue mechanics and transport properties.

Vascularity at this critical interface was also reduced with increasing degeneration, as evidenced by changes in vessel number and area measured via histology and in microFil perfusion to this region. The microvasculature within the rabbit vertebral endplate manifests as vascular buds,(6) which may explain the punctate appearance of the perfused microFil. However, the exact structure of the endplate vasculature may not have been realized by our perfusion technique, due to microFil leakage or inadequate resolution of the μCT scans to resolve connected vessels. MicroFil quantification may also have been affected by vessel bursting in larger upstream vessels or in the networks adjacent to degenerative discs. Additional studies are needed to verify the fidelity of microFil casting of the endplate vascular buds. Our findings do show, however, a reduction in microFil content in endplates adjacent to degenerative discs compared with healthy controls of the same animal perfused in the same fashion, in agreement with our histologic findings. This suggests that there is a hindrance to perfusion in endplates that are adjacent to degenerative discs.

These structure–function alterations in the endplate likely contributed to significant reductions in small molecule diffusion into the NP, as measured via quantitative post-contrast enhanced MRI. Our machine-learning approach, in which 23 structure–function measurements across the endplate, interfaces, AF, and NP tissues from 42 samples were input into a neural network model, identified small molecule transport into the NP as the most important predictor of disc degeneration, further highlighting the importance of trans-endplate transport in disease etiology. The relatively small sample size for the machine-learning model is a limitation of the current work. Despite this, seven of the eight top predictors of histology score from this model also yielded significant and strong correlations via a more traditional Pearson correlation analysis. Additional samples and time points will need to be added in future studies to confirm the findings of the machine-learning approach presented here.

These results build on previous work in the field that has investigated the potential role of endplate sclerosis and altered trans-endplate transport in degeneration. Several studies have indicated that surgical disruption or blockage of the blood supply to the vertebral endplate significantly reduced small molecule transport into the disc and resulted in degenerative changes within the NP.(19,46) In cadaveric human specimens, occlusion of the vertebral endplate marrow channels correlated with the severity of disc degeneration,(47) and structural remodeling of the cartilaginous endplate reduces tissue permeability and is associated with disc degeneration.(48) Vertebral endplate sclerosis may be initiated by altered mechanical loading in the spine, as previous studies have demonstrated endplate changes concomitant with disc degeneration at levels adjacent to a spinal fusion in a rabbit model and in a mouse spinal instability model.(49,50) Our data are in agreement with this hypothesis, as we have previously shown hypermobility of the rabbit lumbar motion segment at early time points after puncture.(24)

With altered endplate transport properties, deleterious molecules, such as lactic acid, are unable to leave the disc and accumulate in the NP, reducing pH and adversely impacting cell function and viability.(9,17) Indeed, Wong and colleagues recently showed that anabolic gene expression was downregulated, and catabolic gene expression was upregulated in NP cells cultured adjacent to cartilage endplates with reduced diffusivity. This supports that low-nutrient diffusion through the endplate limits the number of disc cells that can sustain tissue homeostasis.(18)

This work not only furthers our understanding of the role of endplate remodeling and trans-endplate transport in disc degeneration but also has important implications for clinical diagnosis and treatment. For instance, numerous studies have considered the injection of progenitor cell populations into NP, either alone or within a hydrogel carrier, to improve function.(51) Although this has shown some efficacy in animal models,(52,53) animal discs are a fraction of the size of human lumbar discs and are therefore less nutritionally challenged. In humans, a reduction in diffusion into the disc is likely to adversely impact the viability and metabolic activity of delivered cells,(10) thus reducing their regenerative potential. To maximize the efficacy and clinical translation of such treatments, it may be necessary to first screen patients for trans-endplate transport status before treatment. This could be performed using the post-contrast enhanced MRI method utilized in this study or via other contrast-free techniques, such as ultra-short echo time MRI, which can provide information on the status of the cartilaginous endplate.(54) In patients with compromised diffusion into the disc, it may be necessary to increase trans-endplate transport into the disc in conjunction with cell-based regenerative treatments. This could be achieved via physical therapy exercises to stimulate cyclic compression and distraction of the disc, which has been shown to increase convective transport of small molecules.(30) Alternately, endplate pathology could be targeted with novel therapeutics that are designed to increase vascularity(31) or decrease bone density, thereby enhancing transport potential.

While animal models are essential to study disc degeneration and regeneration, no one model is pathognomonic with human degeneration. Aging models may represent the most “natural” process of degeneration, but a long duration is required to achieve spontaneous degeneration; thus, injury models, as described here, are frequently used.(55) A similar evaluation of the structure–function properties of human discs and endplates must be performed to extend the clinical translatability of this work. Future work should also be performed to evaluate the longer-term biologic consequences of reduced small molecule transport in this model across the disc tissues, and whether any of these deleterious changes are reversed with treatment. Overall, our results demonstrate that reduced small molecule transport into the disc is accompanied by endplate bone and vascular remodeling and is a significant predictor of disc health, warranting increased investigation in this area to improve our understanding of the etiology of degeneration.

Supplementary Material

Refer to Web version on PubMed Central for supplementary material.

Acknowledgments

This work was supported by the National Institute on Aging of the National Institutes of Health (F30 AG060670), the National Institute of Arthritis and Musculoskeletal and Skin Diseases (F32 AR072478), the Penn Center for Musculoskeletal Disorders (NIH, P30 AR069619), and the Department of Veterans Affairs (IK1 RX002445, IK2 RX001476, IK6 RX003416, IK2 RX003118, I01 RX001321, and I01 RX002274). All MRI studies were performed in the University of Pennsylvania Small Animal Imaging Facility.

References

1. Cassidy JJ, Hiltner A, Baer E. Hierarchical structure of the intervertebral disc. Connect Tissue Res. 1989;23(1):75–88. [PubMed: 2632144]
2. Korecki CL, MacLean JJ, Iatridis JC. Dynamic compression effects on intervertebral disc mechanics and biology. Spine. 2008;33(13): 1403–9. [PubMed: 18520935]
3. Fields AJ, Ballatori A, Liebenberg EC, Lotz JC. Contribution of the end-plates to disc degeneration. Curr Mol Biol Rep. 2018;4(4):151–60. [PubMed: 30546999]
4. Huang Y-sC, Urban JPG, Luk KDK. Intervertebral disc regeneration: do nutrients lead the way? Nat Rev Rheumatol. 2014;10(9):561–6. [PubMed: 24914695]
5. Roberts S, Menage J, Urban JPG. Biochemical and structural properties of the cartilage end-plate and its relation to the intervertebral disc. Spine. 1989;14(2):166–74. [PubMed: 2922637]
6. Oki S, Matsuda Y, Shibata T, Okumura H, Desaki J. Morphologic differences of the vascular buds in the vertebral endplate: scanning electron microscopic study. Spine. 1996;21(2):174–7. [PubMed: 8720400]

7. Nachemson A, Lewin T, Maroudas A, Freeman MA. In vitro diffusion ofdye through the end-plates and the annulus fibrosus of human lumbar inter-vertebral discs. Acta Orthop Scand. 1970;41(6):589–607. [PubMed: 5516549]
8. Ratcliffe JF. The arterial anatomy of the adult human lumbar vertebral body: a microarteriographic study. J Anat. 1980;131(1):57–79. [PubMed: 7440404]
9. Urban JPG, Smith S, Fairbank JCT. Nutrition of the intervertebral disc. Spine. 2004;29(23):2700–9. [PubMed: 15564919]
10. Bibby SRS, Urban JPG. Effect of nutrient deprivation on the viability of intervertebral disc cells. Eur Spine J. 2004;13(8):695–701. [PubMed: 15048560]
11. Grunhagen T, Wilde G, Soukane DM, Shirazi-Adl SA, Urban JPG. Nutrient supply and intervertebral disc metabolism. J Bone Joint Surg Am. 2006;88(Suppl 2):30–5. [PubMed: 16595440]
12. An HS, Anderson PA, Haughton VM, et al. Introduction: disc degeneration: summary. Spine. 2004;29(23):2677. [PubMed: 15564916]
13. CDC. Prevalence and most common causes of disability among adults—United States, 2005. MMWR. 2009;58(16):421–6. [PubMed: 19407734]
14. Battié MC, Videman T, Levälahti E, Gill K, Kaprio J. Genetic and environmental effects on disc degeneration by phenotype and spinal level: a multivariate twin study. Spine. 2008;33(25):2801–8. [PubMed: 19050586]
15. Fearing BV, Hernandez PA, Setton LA, Chahine NO. Mechanotransduction and cell biomechanics of the intervertebral disc. JOR Spine. 2018;1(3):e1026.
16. Annunen S, Paassilta P, Lohiniva J, et al. An allele of COL9A2 associated with intervertebral disc disease. Science. 1999;285(5426): 409–12. [PubMed: 10411504]
17. Roberts S, Urban JP, Evans H, Eisenstein SM. Transport properties of the human cartilage endplate in relation to its composition and calcification. Spine. 1996;21(4):415–20. [PubMed: 8658243]
18. Wong J, Sampson SL, Bell-Briones H, et al. Nutrient supply and nucleus pulposus cell function: effects of the transport properties of the cartilage endplate and potential implications for intradiscal biologic therapy. Osteoarthritis Cartilage. 2019;27(6):956–64. [PubMed: 30721733]
19. van der Werf M, Lezuo P, Maissen O, van Donkelaar CC, Ito K. Inhibition of vertebral endplate perfusion results in decreased intervertebral disc intranuclear diffusive transport. J Anat. 2007;211(6):769–74. [PubMed: 17953653]
20. Boos N, Weissbach S, Rohrbach H, Weiler C, Spratt KF, Nerlich AG. Classification of age-related changes in lumbar intervertebral discs: 2002 Volvo Award in basic science. Spine. 2002;27(23):2631–44. [PubMed: 12461389]
21. Rodriguez AG, Rodriguez-Soto AE, Burghardt AJ, Berven S, Majumdar S, Lotz JC. Morphology of the human vertebral endplate. J Orthop Res. 2012;30(2):280–7. [PubMed: 21812023]
22. Kaiser J, Allaire B, Fein PM, et al. Correspondence between bone mineral density and intervertebral disc degeneration across age and sex. Arch Osteoporos. 2018;13(1):123. [PubMed: 30421154]
23. Kauppila LI. Atherosclerosis and disc degeneration/low-back pain—a systematic review. Eur J Vasc Endovasc Surg. 2009;37(6):661–70. [PubMed: 19328027]
24. Ashinsky BG, Gullbrand SE, Bonnevie ED, et al. Multiscale and multimodal structure-function analysis of intervertebral disc degeneration in a rabbit model. Osteoarthritis Cartilage. 2019;27(12):1860–9. [PubMed: 31419488]
25. Masuda K, Aota Y, Muehleman C, et al. A novel rabbit model of mild, reproducible disc degeneration by an anulus needle puncture: correlation between the degree of disc injury and radiological and histological appearances of disc degeneration. Spine. 2005;30(1):5–14. [PubMed: 15626974]
26. Gullbrand SE, Malhotra NR, Schaer TP, et al. A large animal model that recapitulates the spectrum of human intervertebral disc degeneration. Osteoarthritis Cartilage. 2017;25(1):146–56. [PubMed: 27568573]
27. van Gaalen SM, Kruyt MC, Geuze RE, de Bruijn JD, Alblas J, Dhert WJA. Use of fluorochrome labels in in vivo bone tissue engineering research. Tissue Eng Part B Rev. 2010;16(2):209–17. [PubMed: 19857045]

28. Spicer PP, Kretlow JD, Young S, Jansen JA, Kasper FK, Mikos AG. Evaluation of bone regeneration using the rat critical size calvarial defect. Nat Protoc. 2012;7(10):1918–29. [PubMed: 23018195]
29. Kawamoto T, Shimizu M. A method for preparing whole-body sections suitable for autoradiographic, histological and histochemical studies. Stain Technol. 1986;61(3):169–83. [PubMed: 3523839]
30. Gullbrand SE, Peterson J, Ahlborn J, et al. ISSLS prize winner: dynamic loading-induced convective transport enhances intervertebral disc nutrition. Spine. 2015;40(15):1158–64. [PubMed: 26222661]
31. Gullbrand SE, Peterson J, Mastropolo R, et al. Drug-induced changes to the vertebral endplate vasculature affect transport into the intervertebral disc in vivo. J Orthop Res. 2014;32(12):1694–700. [PubMed: 25185989]
32. Rajasekaran S, Babu JN, Arun R, Armstrong BRW, Shetty AP, Murugan S. ISSLS prize winner: a study of diffusion in human lumbar discs: a serial magnetic resonance imaging study documenting the influence of the endplate on diffusion in normal and degenerate discs. Spine. 2004;29(23):2654–67. [PubMed: 15564914]
33. Pickup S, Wood AKW, Kundel HL. Gadodiamide T1 relaxivity in braint issue in vivo is lower than in saline. Magn Reson Med. 2005;53(1): 35–40. [PubMed: 15690500]
34. Li Q, Qu F, Han B, et al. Micromechanical anisotropy and heterogeneity of the meniscus extracellular matrix. Acta Biomater. 2017;54: 356–66. [PubMed: 28242455]
35. Riebel GD, Boden SD, Whitesides TE, Hutton WC. The effect of nicotine on incorporation of cancellous bone graft in an animal model. Spine. 1995;20(20):2198–202. [PubMed: 8545712]
36. Cason JE. A rapid one-step Mallory-Heidenhain stain for connective tissue. Stain Technol. 1950;25(4):225–6. [PubMed: 14782060]
37. Gullbrand SE, Schaer TP, Agarwal P, et al. Translation of an injectable triple-interpenetrating-network hydrogel for intervertebral disc regeneration in a goat model. Acta Biomater. 2017;60:201–9. [PubMed: 28735027]
38. Gullbrand SE, Ashinsky BG, Bonnevie ED, et al. Long-term mechanical function and integration of an implanted tissue-engineered intervertebral disc. Sci Transl Med. 2018;21(10):468.
39. Liu Y, Gopalakrishnan V. An overview and evaluation of recent machine learning imputation methods using cardiac imaging data. Data. 2017;2(1):8. [PubMed: 28243594]
40. Madelin G, Poidevin F, Makrymallis A, Regatte RR. Classification of sodium MRI data of cartilage using machine learning. Magn Reson Med. 2015;74(5):1435–48. [PubMed: 25367844]
41. Aoki Y, Akeda K, An H, et al. Nerve fiber ingrowth into scar tissue formed following nucleus pulposus extrusion in the rabbit anular-puncture disc degeneration model: effects of depth of puncture. Spine. 2006;31(21):E774–80. [PubMed: 17023838]
42. Miyamoto K, Masuda K, Kim JG, et al. Intradiscal injections of osteogenic protein-1 restore the viscoelastic properties of degenerated intervertebral discs. Spine J. 2006;6(6):692–703. [PubMed: 17088200]
43. Sobajima S, Kompel JF, Kim JS, et al. A slowly progressive and reproducible animal model of intervertebral disc degeneration characterized by MRI, X-ray, and histology. Spine. 2005;30(1):15–24. [PubMed: 15626975]
44. Armitage OE, Oyen ML. Indentation across interfaces between stiff and compliant tissues. Acta Biomater. 2017;56:36–43. [PubMed: 28062353]
45. Fields AJ, Rodriguez D, Gary KN, Liebenberg EC, Lotz JC. Influence of biochemical composition on endplate cartilage tensile properties in the human lumbar spine. J Orthop Res. 2014;32(2):245–52. [PubMed: 24273192]
46. Yuan W, Che W, Jiang Y-Q, et al. Establishment of intervertebral disc degeneration model induced by ischemic sub-endplate in rat tail. Spine J. 2015;15(5):1050–9. [PubMed: 25637466]
47. Benneker LM, Heini PF, Alini M, Anderson SE, Ito K. 2004 Young Investigator Award winner: vertebral endplate marrow contact channel occlusions and intervertebral disc degeneration. Spine. 2005;30(2): 167–73. [PubMed: 15644751]

48. DeLucca JF, Cortes DH, Jacobs NT, Vresilovic EJ, Duncan RL, Elliott DM. Human cartilage endplate permeability varies with degeneration and intervertebral disc site. J Biomech. 2016;49(4):550–7. [PubMed: 26874969]
49. Phillips FM, Reuben J, Wetzel FT. Intervertebral disc degeneration adjacent to a lumbar fusion. An experimental rabbit model. J Bone Joint Surg Br. 2002;84(2):289–94. [PubMed: 11922374]
50. Bian Q, Jain A, Xu X, et al. Excessive activation of TGFβ by spinal instability causes vertebral endplate sclerosis. Sci Rep. 2016;3(6):27093.
51. Vickers L, Thorpe AA, Snuggs J, Sammon C, Le Maitre CL. Mesenchymal stem cell therapies for intervertebral disc degeneration: consideration of the degenerate niche. JOR Spine. 2019;2(2):e1055.
52. Hiraishi S, Schol J, Sakai D, et al. Discogenic cell transplantation directly from a cryopreserved state in an induced intervertebral disc degeneration canine model. JOR Spine. 2018;1(2):e1013.
53. Shu CC, Dart A, Bell R, et al. Efficacy of administered mesenchymal stem cells in the initiation and coordination of repair processes by resident disc cells in an ovine (Ovis aries) large destabilizing lesion model of experimental disc degeneration. JOR Spine. 2018;1(4):e1037.
54. Berg-Johansen B, Han M, Fields AJ, et al. Cartilage endplate thickness variation measured by ultrashort echo-time MRI is associated with adjacent disc degeneration. Spine. 2018;43(10):E592–600. [PubMed: 28984733]
55. Daly C, Ghosh P, Jenkin G, Oehme D, Goldschlager T. A review of animal models of intervertebral disc degeneration: pathophysiology, regeneration, and translation to the clinic. Biomed Res Int. 2016; 2016:5952–165.

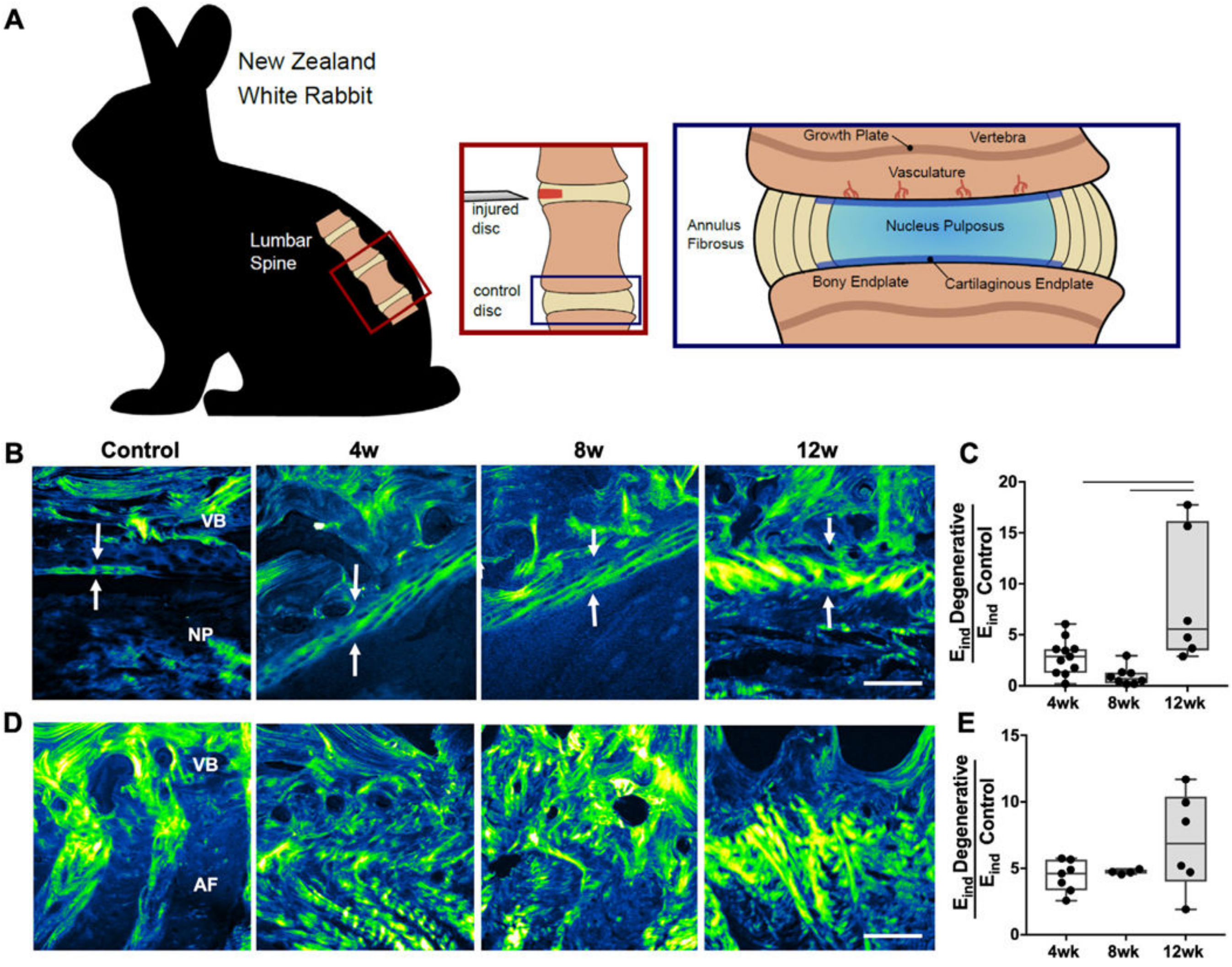

Fig. 1.

(*A*) Schematic depicting the surgical approach for the disc puncture model and regions of the spinal motion segment investigated in this study. (*B*) Second harmonic generation imaging (SHG) of the cartilaginous endplate between the vertebral endplate and nucleus pulposus and (C) corresponding indentation modulus (E_{ind}) of this region, normalized to control values. (*D*) SHG of the vertebral endplate-AF region and corresponding E_{ind} of this region, normalized to control values. Arrows indicate cartilage endplate thickness. VB = vertebral body; NP = nucleus pulposus; AF = annulus fibrosus. Scale bar = 100 μm. Bars denote statistical significance (4 to 12 weeks, $p = 0.008$; 8 to 12 weeks, $p = 0.001$), Kruskal-Wallis test.

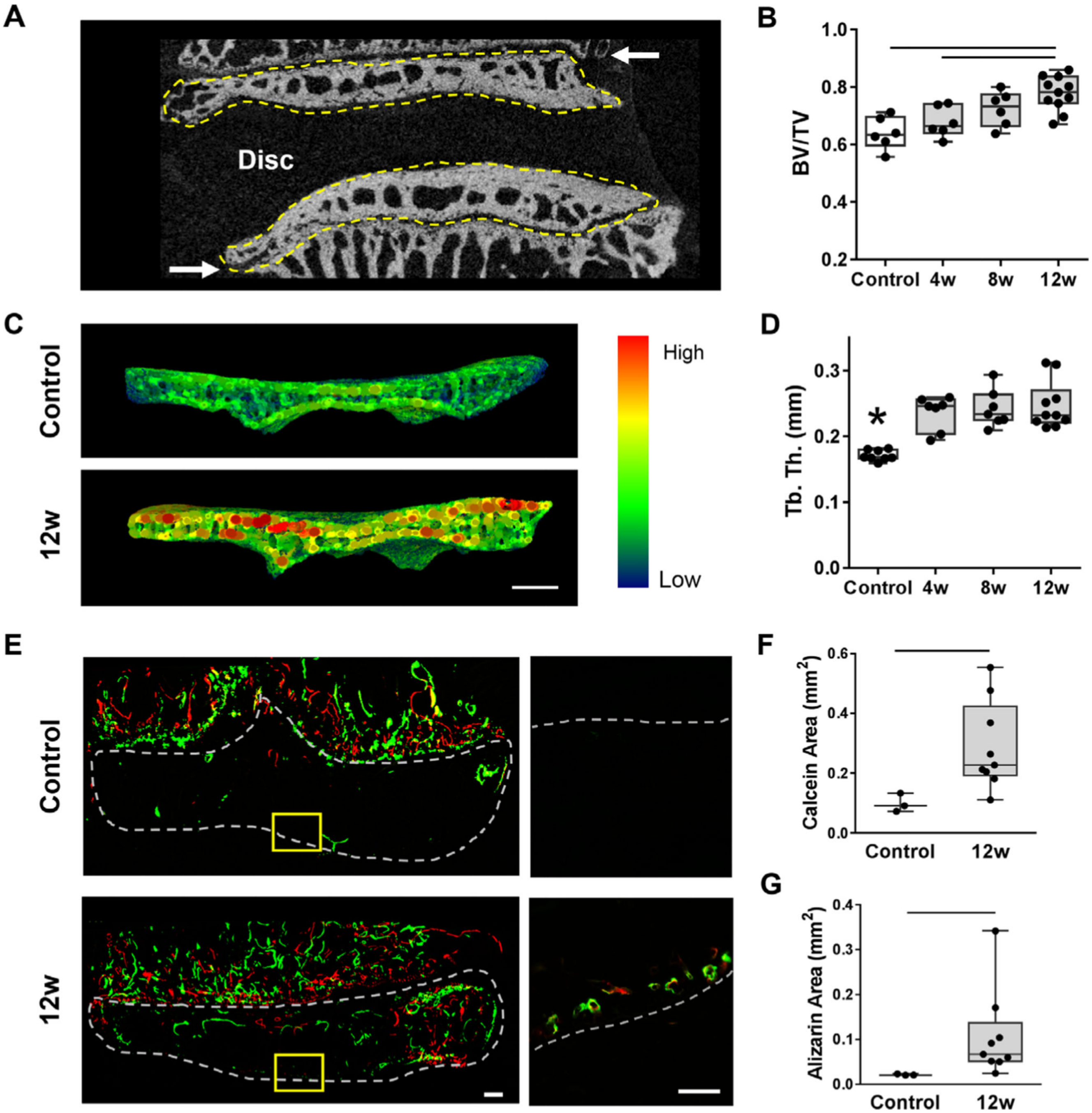

Fig. 2.

(*A*) Representative mid-coronal μCT slice of a control motion segment, with the cranial and caudal vertebral endplates outlined in yellow, denoting the volume of interest analyzed for bone morphometry. Arrows indicate the growth plates. (*B*) Quantification of bone volume/ total volume (BV/TV) in the endplate regions for each group. (*C*) Representative trabecular thickness (Tb.Th) map of the endplate volume of interest and (*D*) corresponding quantification of Tb.Th of the endplates in each group. (*E*) Representative images of the bone fluorochrome labels (calcein = green, alizarin = red) in the endplate region. The dashed outline in the macroscale image denotes the endplate region between the disc and growth plate (scale bar = 100 μm). In the inset images (scale bar = 100 μm), the dashed line denotes the border between the NP and the endplate. (*F*) Quantification of calcein and alizarin areas in the control and 12-week punctured groups. Bars denote statistical significance (BV/TV = control-12 weeks, $p = 0.0004$; 4–12 weeks, $p = 0.01$; Tb.Th = control-4 weeks, $p = 0.0006$; control-8 weeks, $p = 0.0002$; control-12 weeks, $p < 0.0001$, ANOVA). Calcein: $p = 0.01$; alizarin: $p = 0.009$, Mann–Whitney test.

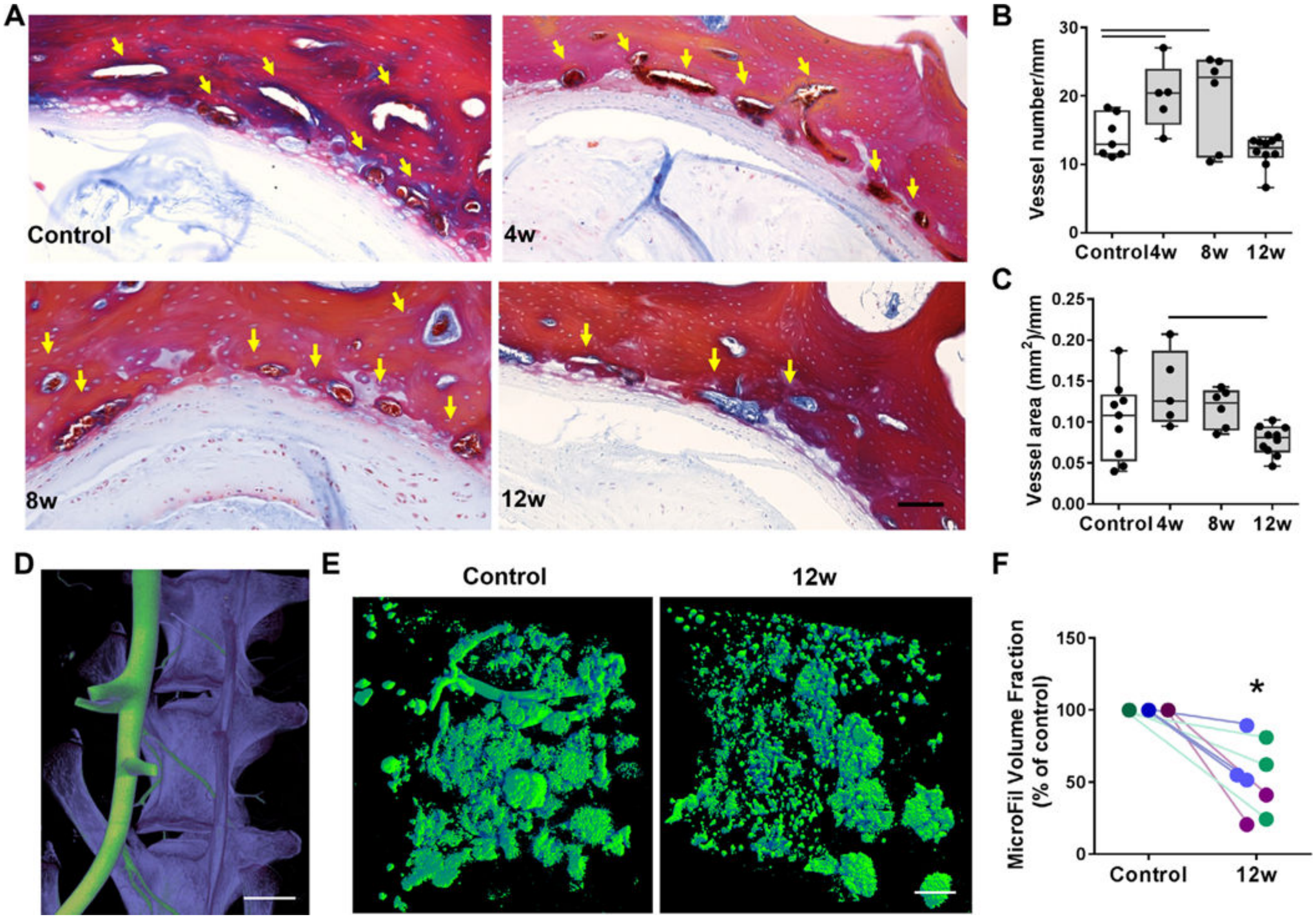

Fig. 3.

(*A*) Mallory-Heidenhain staining of histology sections for the endplate vasculature; arrows indicate vessels. Scale bar = 100 μm. (*B*) Quantification of vessel number and (*C*) area normalized to endplate length adjacent to the NP. 3D μCT reconstructions of the (*D*) spinal vasculature perfused with microFil (green) and the vertebral bodies (purple) before decalcification (scale bar = 5 mm) and (*E*) microFil perfusion of the small vasculature adjacent to the disc, visualized after decalcification (scale bar = 500 μm). (*F*) MicroFil volume fraction in the endplate adjacent to degenerative discs 12 weeks post-puncture compared with controls (each color indicates separate animal). Bars denote statistical significance (vessel area = control-4 weeks, $p = 0.01$; 4–8 weeks, $p = 0.009$; vessel number = $p = 0.03$), Kruskal-Wallis test.

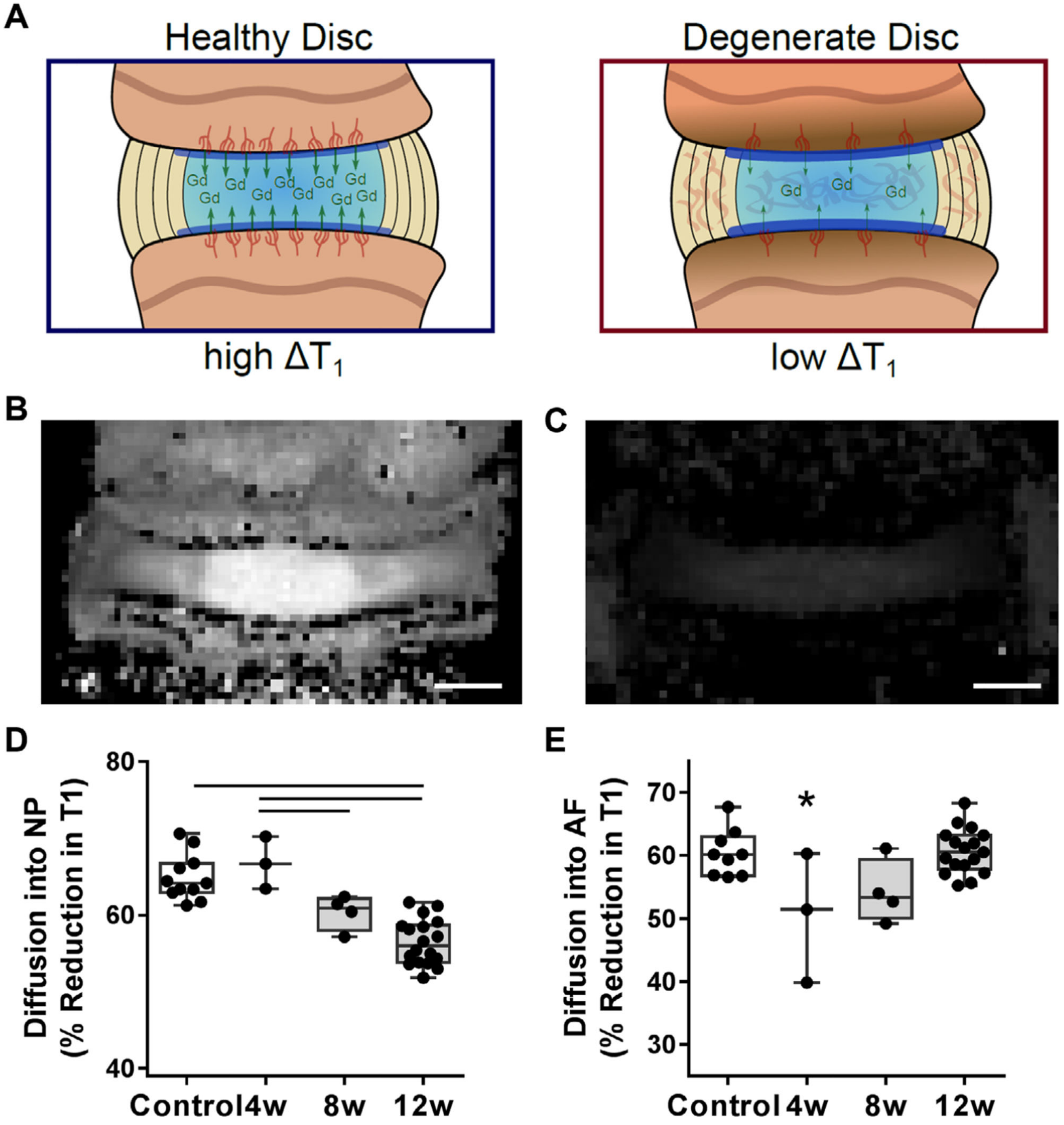

Fig. 4.

(*A*) Schematic depicting the change in T_1 relaxation time within the intervertebral disc after administration of the contrast agent gadodiamide (Gd). Representative MRI T_1 maps of a control disc (*B*) before and (*C*) after administration of Gd, demonstrating the reduction in T1 relaxation time (scale bar = 1 mm). (*D*) The percent reduction in T_1 into the NP and (*E*) AF after Gd administration in each experimental group. Bars denote statistical significance (%T1 NP = control-12 weeks, $p < 0.0001$; 4–8 weeks, $p = 0.03$; 4–12 weeks, $p < 0.0001$; %T1 AF = control-4 weeks, $p = 0.01$; 4–12 weeks, $p = 0.006$), ANOVA.

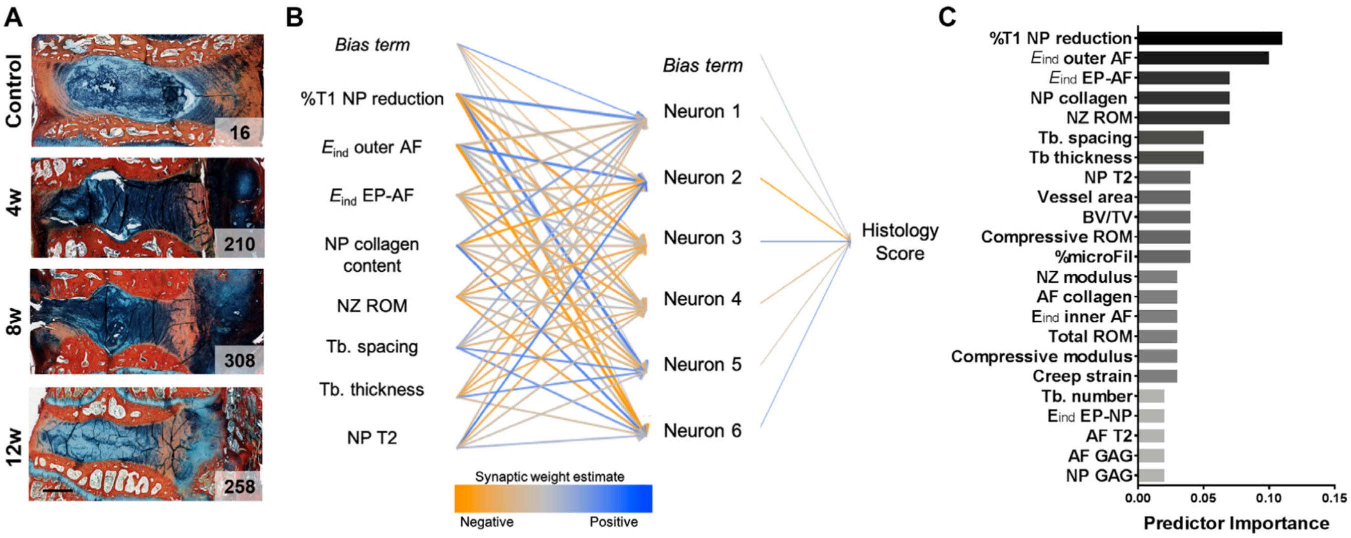

Fig. 5.

(*A*) Representative Alcian blue and picrosirius red stained sections from each experimental group, with total histology score indicated on each image (scale bar = 2 mm). (*B*) A neural network model was utilized to predict histology score based on 23 input parameters of disc structure and function (the top eight predictors are shown). (*C*) Relative predictor importance for all input parameters.